



CERN-EP-2019 -XXX  
Day Month 2019

## $\Lambda K$ femtoscopy in Pb-Pb collisions at $\sqrt{s_{NN}} = 2.76$ TeV

ALICE Collaboration\*

### Abstract

The first measurements of the scattering parameters of  $\Lambda K$  pairs in all three charge combinations ( $\Lambda K^+$ ,  $\Lambda K^-$ , and  $\Lambda K_S^0$ ) are presented. The measurements are achieved through a femtoscopic analysis of  $\Lambda K$  correlations in Pb-Pb collisions at  $\sqrt{s_{NN}} = 2.76$  TeV from ALICE at the LHC. The femtoscopic correlations result from strong final-state interactions, and are fit with a parametrization allowing for both the characterization of the pair emission source and the measurement of the scattering parameters for the particle pairs. Extensive studies with the THERMINATOR 2 event generator allow for the description of the non-femtoscopic background, resulting mainly from collective effects, with unprecedented precision. Furthermore, this model together with HIJING simulations are used to account for contributions from residual correlations induced by feed-down from resonances. The  $\Lambda K^+$  system exhibits a negative real component of the scattering parameter ( $\Re f_0$ ), while those of the  $\Lambda K^-$  and  $\Lambda K_S^0$  are positive, although the magnitude of that of the  $\Lambda K_S^0$  is smaller than that of the  $\Lambda K^-$ . The results suggest an effect arising from different quark-antiquark interactions between the pairs ( $s\bar{s}$  in  $\Lambda K^+$  and  $u\bar{u}$  in  $\Lambda K^-$ ), or from different net strangeness for each system ( $S=0$  for  $\Lambda K^+$ , and  $S=-2$  for  $\Lambda K^-$ ). Finally, the  $\Lambda K$  systems exhibit source radii larger than expected from extrapolation from identical particle femtoscopic studies. This effect is interpreted as resulting from the separation in space-time of the single-particle  $\Lambda$  and  $K$  source distributions.

## 1 Introduction

Femtoscopy is an experimental method used to study the space-time characteristic of the particle emitting sources in relativistic particle collisions [1]. With this method, two (or many)-particle relative-momentum correlation functions are used to connect the final-state momentum distributions to the space-time distributions of particle emission at freeze-out. The correlation functions are sensitive to quantum statistics, as well as strong and Coulomb final-state interactions (FSI). Current femtoscopic studies are able to extract the size, shape, and orientation of the pair emission regions, as well as offering estimations of the total time to reach kinetic decoupling and the suddenness of particle emission. Non-identical particle analyses additionally allow for the measurement of the space-time separation of the single particle source emitting regions. The momentum and species dependence of femtoscopic measurements affirm the collective nature of the hot and dense matter created in heavy-ion collisions.

In addition to characterizing the source region, femtoscopy offers a unique environment in which to measure nuclear scattering parameters, many of which are difficult, if not impossible, to measure otherwise. This aspect of femtoscopy is the focal point of the present analysis. In this analysis, Λ-K pairs are studied, in which at least one particle is electrically neutral. Quantum statistics and the Coulomb interaction do not contribute, offering a clear signal from the strong interaction.

Calculations within Quantum Chromodynamics (QCD), the theory of the strong interaction, are notoriously difficult except in select regimes of weak coupling, where perturbative methods may be applied. The ΛK analysis presented offers low energy QCD measurements, which fall into the non-perturbative regime of QCD. Therefore, the ΛK measurements not only give insight into the strong interaction, they will also help guide future QCD calculations. This study is also particularly interesting, as the ΛK scattering parameters are not known, and therefore the behavior of the system cannot be predicted beforehand. Scattering parameters for similar systems are also very limited; past studies of kaon-proton scattering revealed the strong force is attractive in the  $K^-p$  interaction, and repulsive in that of the  $K^+p$  [2–4].

This paper presents the first measurements of the scattering parameters of ΛK pairs in all three charge combinations ( $\Lambda K^+$ ,  $\Lambda K^-$ , and  $\Lambda K_S^0$ ). The scattering parameters, along with pair emission source sizes, are extracted with a femtoscopic analysis of ΛK correlations in Pb-Pb collisions at  $\sqrt{s_{NN}} = 2.76$  TeV from the ALICE experiment at the LHC. These correlations result from strong final-state interactions, and are fit with a parametrization by Lednický and Lyuboshitz [5]. Extensive studies with the THERMINATOR 2 event generator are performed to account for both non-femtoscopic backgrounds, as well as contributions from residual correlations induced by feed-down from resonances.

The organization of this paper is as follows. In Sec. 2 the data selection methods are briefly discussed. In Sec. 3 the analysis techniques utilized in this study are presented. Here, the two particle correlation function is introduced, as well as the theoretical models with which the data are fit. This section also includes descriptions of the handling of residual correlations, corrections accounting for finite track momentum resolution, treatment of the non-femtoscopic background, as well as a brief description of the systematic uncertainties estimation. The final results are presented in Sec. 4, and concluding remarks are given in Sec. 5. Appendix A demonstrates an alternate approach to forming correlation functions, whose purpose here is to help eliminate the non-femtoscopic background. Appendix B discusses the procedure needed to generate fit functions when both the strong and Coulomb interactions are present. In Appendix C, the THERMINATOR 2 event generator is used to demonstrate the effect of increasing the source offset in the “out” direction ( $\mu_{out}$ ) on a one-dimensional femtoscopic fit. Throughout the text, the pair name is used as shorthand for the pair-conjugate system, which are found to be consistent (e.g.  $\Lambda K_S^0$ ,  $\Lambda K^+ \oplus \bar{\Lambda} K^-$  is simply  $\Lambda K^+$ ).

## 2 Data Analysis

The dataset analyzed is from Pb-Pb collisions at  $\sqrt{s_{\text{NN}}} = 2.76$  TeV at the LHC measured by the ALICE detector [6] in 2011. Approximately 40 million combined central, semi-central, and minimum bias events were analyzed. The events were classified according to their centrality determined using the measured amplitudes in the V0 detectors [7]. In order for an event to be included in the analysis, the z-position of the reconstructed event vertex must be within 10 cm of the center of the ALICE detector, and the event must contain at least one particle of each type from the pair of interest (e.g. for  $\Lambda K_S^0$  analysis, an accepted event must contain at least one  $\Lambda$  and at least one  $K_S^0$ ).

Charged particle tracking was performed using the Time Projection Chamber (TPC) [8] and the Inner Tracking System [9]. The ITS allows for high spatial resolution in determining the primary (collision) vertex. The determination of the momenta of the tracks was performed using tracks reconstructed with the TPC only and constrained to the primary vertex. A minimum requirement of 80 reconstructed TPC clusters was imposed, the purpose of which is to ensure both the quality of the track and good  $p_T$  resolution at large momenta, as well as to remove fake tracks.

Particle identification (PID) for reconstructed tracks was carried out using both the TPC and Time-of-Flight (TOF) detector [10, 11] in the pseudorapidity range  $|\eta| < 0.8$ . For TPC PID, a parametrized Bethe-Bloch formula was used to calculate the specific energy loss  $\langle dE/dx \rangle$  in the detector expected for a particle with a given mass and momentum. For TOF PID, the particle mass was used to calculate the expected time-of-flight as a function of track length and momentum. For each PID method, a value ( $N_\sigma$ ) was assigned to each track denoting the number of standard deviations between the measured track information and calculated values. This procedure was repeated for four “particle species hypotheses”—electron, pion, kaon, and proton—, and for each hypothesis a different  $N_\sigma$  value was obtained per detector.

### 2.1 $K^\pm$ selection

The single-particle selection criteria used to select charged kaon candidates are summarized in Table 1.  $K^\pm$  track detection utilized both TPC and TOF detectors, and tracks within the range  $0.14 < p_T < 1.5$  GeV/c were accepted. To reduce the number of secondaries (e.g. charged particles produced in the detector material, particles from weak decays, etc.) in the sample, a maximum cut is established on the distance-of-closest-approach (DCA) of the track to the primary vertex. This restriction is realized by imposing a DCA cut in both the transverse and beam directions.

PID was performed using both the TPC and TOF detectors via the  $N_\sigma$  method. The  $N_\sigma$  cuts become tighter with increasing momentum to reduce contamination within the samples, as the  $K^\pm$  signals begin to overlap more significantly with those from other particles, particularly  $e^\pm$  and  $\pi^\pm$ . Additional methods are included to reduce the contamination in the  $K^\pm$  samples from the electrons and pions. The specifics for these cuts are contained in Table 1. The purity of the  $K^\pm$  collections,  $P_{K^\pm}$ , was estimated to be approximately 97% from a Monte-Carlo (MC) study based on HIJING [12] simulations using GEANT3 [13] to model particle transport through the ALICE detectors. For a more detailed estimate of the  $K^\pm$  purity from an analysis employing similar cuts, see Ref. [14].

### 2.2 $V^0$ selection

$\Lambda$  ( $\bar{\Lambda}$ ) and  $K_S^0$  particles are reconstructed through their weak decays:  $\Lambda \rightarrow p\pi^-$  ( $\bar{\Lambda} \rightarrow \pi^+\bar{p}$ ) and  $K_S^0 \rightarrow \pi^+\pi^-$ . The obtained candidates are denominated as  $V^0$  particles. The main cuts used are shown in Tables 2 and 3.

Aside from typical kinematic and PID cuts (using TPC and TOF detectors), the daughter tracks are also exposed to a minimum cut on their impact parameter with respect to the primary vertex. The decay vertex of the  $V^0$  is assumed to be the point of closest approach between the daughter tracks. To help ensure

K <sup>±</sup> selection		
Transverse momentum $p_T$		$0.14 < p_T < 1.5 \text{ GeV}/c$
$ \eta $		$< 0.8$
Transverse DCA to primary vertex		$< 2.4 \text{ cm}$
Longitudinal DCA to primary vertex		$< 3.0 \text{ cm}$
TPC and TOF $N_\sigma$ Cuts		
$p < 0.4 \text{ GeV}/c$		$N_{\sigma K, \text{TPC}} < 2$
$0.4 \leq p < 0.45 \text{ GeV}/c$		$N_{\sigma K, \text{TPC}} < 1$
$0.45 \leq p < 0.80 \text{ GeV}/c$		$N_{\sigma K, \text{TPC}} < 3$ $N_{\sigma K, \text{TOF}} < 2$
$0.80 \leq p < 1.0 \text{ GeV}/c$		$N_{\sigma K, \text{TPC}} < 3$ $N_{\sigma K, \text{TOF}} < 1.5$
$p \geq 1.0 \text{ GeV}/c$		$N_{\sigma K, \text{TPC}} < 3$ $N_{\sigma K, \text{TOF}} < 1$
Electron Rejection: Reject if all satisfied		$N_{\sigma e^-, \text{TPC}} < 3$ $N_{\sigma e^-, \text{TPC}} < N_{\sigma K^\pm, \text{TPC}}$ $N_{\sigma e^-, \text{TOF}} < N_{\sigma K^\pm, \text{TOF}}$
Pion Rejection: Reject if:		
$p < 0.65 \text{ GeV}/c$	TOF and TPC available	
	$N_{\sigma \pi, \text{TPC}} < 3$ $N_{\sigma \pi, \text{TOF}} < 3$	
	Only TPC available	$p < 0.5 \text{ GeV}/c$
		$0.5 \leq p < 0.65 \text{ GeV}/c$
		$N_{\sigma \pi, \text{TPC}} < 3$ $N_{\sigma \pi, \text{TPC}} < 2$
$0.65 \leq p < 1.5 \text{ GeV}/c$		$N_{\sigma \pi, \text{TPC}} < 5$ $N_{\sigma \pi, \text{TOF}} < 3$
$p \geq 1.5 \text{ GeV}/c$		$N_{\sigma \pi, \text{TPC}} < 5$ $N_{\sigma \pi, \text{TOF}} < 2$

**Table 1:** K<sup>±</sup> selection

quality, a maximum value cut is demanded on the distance-of-closest-approach between the daughters (DCA  $V^0$  Daughters). The positive and negative daughter tracks are combined to form the  $V^0$  candidate, the momentum of which is simply the sum of the momenta of the daughters (calculated at the DCA).

To select primary candidates, each  $V^0$  is exposed to a maximum cut on its impact parameter with respect to the primary vertex. Furthermore, a selection is imposed on the pointing angle,  $\theta_{pa}$ , between the  $V^0$  momentum and the vector pointing from the primary vertex to the secondary  $V^0$  decay vertex, which is achieved by appointing a minimum value on  $\cos(\theta_{pa})$  (“Cosine of pointing angle” in Tables 2 and 3).

In order to remove the contamination to the  $\Lambda$  ( $\bar{\Lambda}$ ) and  $K_S^0$  samples due to misidentification of the protons and pions for each  $V^0$ , the mass assuming different identities ( $\Lambda$ ,  $\bar{\Lambda}$ ,  $K_S^0$ )<sup>1</sup> is calculated and utilized in a set of misidentification cuts. For  $\Lambda$  ( $\bar{\Lambda}$ ) selection, a candidate is assumed to be misidentified and is rejected if all of the following criteria are satisfied:

1.  $|m_{inv, K_S^0 \text{ hyp.}} - m_{PDG, K_S^0}| < 9.0 \text{ MeV}/c^2$
2. The daughter particles pass daughter cuts intended for  $K_S^0$  reconstruction
3.  $|m_{inv, K_S^0 \text{ hyp.}} - m_{PDG, K_S^0}| < |m_{inv, \Lambda(\bar{\Lambda}) \text{ hyp.}} - m_{PDG, \Lambda(\bar{\Lambda})}|$

Similarly, for  $K_S^0$  selection, a candidate is rejected if all of the following criteria are satisfied for the  $\Lambda$  case, or for the  $\bar{\Lambda}$  case:

1.  $|m_{inv, \Lambda(\bar{\Lambda}) \text{ hyp.}} - m_{PDG, \Lambda(\bar{\Lambda})}| < 9.0 \text{ MeV}/c^2$
2. The daughter particles pass daughter cuts intended for  $\Lambda$  ( $\bar{\Lambda}$ ) reconstruction
3.  $|m_{inv, \Lambda(\bar{\Lambda}) \text{ hyp.}} - m_{PDG, \Lambda(\bar{\Lambda})}| < |m_{inv, K_S^0 \text{ hyp.}} - m_{PDG, K_S^0}|$

A final cut on the invariant mass ( $m_{inv}$ ) is applied to enhance the purity. These cuts are shown in Tables 2 and 3. Finally, to avoid any auto-correlation effects, all  $V^0$  candidates are ensured to have unique daughters. If a daughter is found to be shared between  $V^0$  candidates, only the candidate with the smallest DCA to the primary vertex is kept. The resulting invariant mass distributions for  $\Lambda$  and  $K_S^0$  collections in the 0–10% centrality bin are shown in Figure 1. For the purity estimations, the background signal is estimated by fitting the  $m_{inv}$  distribution outside of the mass peak and assuming the distribution to continue smoothly within the mass peak. The  $\Lambda$  and  $\bar{\Lambda}$  purities are estimated to be  $P_{\Lambda(\bar{\Lambda})} \approx 95\%$ , and that of the  $K_S^0$  is  $P_{K_S^0} \approx 98\%$ .

### 2.3 Pair Construction

In order to reduce the contamination to the two-particle correlations due to pairs sharing daughters and to split or merged tracks, two main pair cuts are applied: a shared daughter cut, and an average separation cut. The purpose of the shared daughter cut is to ensure the first particle in the pair is unique from the second. For pairs formed of two  $V^0$ s (i.e.  $\Lambda K_S^0$ ), this cut is implemented by removing all pairs which share a daughter. For a pair formed of a single  $V^0$  and a charged track (i.e.  $\Lambda K^\pm$ ), the cut removes all pairs in which the charged track is also claimed as a daughter of the  $V^0$ .

<sup>1</sup> For the misidentification cuts, the mass assuming  $K_S^0$  hypothesis ( $m_{inv, K_S^0 \text{ hyp.}}$ ) is calculated assuming  $\pi^+\pi^-$  daughters, the mass assuming  $\Lambda$  hypothesis ( $m_{inv, \Lambda \text{ hyp.}}$ ) is calculated assuming  $p\pi^-$  daughters, and the mass assuming  $\bar{\Lambda}$  hypothesis ( $m_{inv, \bar{\Lambda} \text{ hyp.}}$ ) is calculated assuming  $\bar{p}\pi^+$  daughters. Additionally,  $m_{PDG, K_S^0}$  and  $m_{PDG, \Lambda(\bar{\Lambda})}$  denote the particle masses of the  $K_S^0$  and  $\Lambda$  ( $\bar{\Lambda}$ ), respectively, as recorded by the Particle Data Group [15].

Λ selection	
Transverse momentum $p_T$	$> 0.4 \text{ GeV}/c$
$ \eta $	$< 0.8$
Invariant mass	$ m_{p\pi} - m_{PDG}  < 3.8 \text{ MeV}/c^2$
DCA to primary vertex	$< 0.5 \text{ cm}$
Cosine of pointing angle	$> 0.9993$
Decay Length	$< 60 \text{ cm}$
Daughter Cuts ( $\pi$ and $p$ )	
$ \eta $	$< 0.8$
DCA $\pi p$ Daughters	$< 0.4 \text{ cm}$
$\pi$ -specific cuts	
$p_T$	$> 0.16 \text{ GeV}/c$
DCA to primary vertex	$> 0.3 \text{ cm}$
TPC and TOF $N_\sigma$ Cuts	
$p < 0.5 \text{ GeV}/c$	$N_{\sigma_{\text{TPC}}} < 3$
$p \geq 0.5 \text{ GeV}/c$	TOF & TPC available $N_{\sigma_{\text{TPC}}} < 3$
	$N_{\sigma_{\text{TOF}}} < 3$
	Only TPC available $N_{\sigma_{\text{TPC}}} < 3$
$p$ -specific cuts	
$p_T$	$> 0.5(p) [0.3(\bar{p})] \text{ GeV}/c$
DCA to primary vertex	$> 0.1 \text{ cm}$
TPC and TOF $N_\sigma$ Cuts	
$p < 0.8 \text{ GeV}/c$	$N_{\sigma_{\text{TPC}}} < 3$
$p \geq 0.8 \text{ GeV}/c$	TOF & TPC available $N_{\sigma_{\text{TPC}}} < 3$
	$N_{\sigma_{\text{TOF}}} < 3$
	Only TPC available $N_{\sigma_{\text{TPC}}} < 3$

**Table 2:** Λ selection

$K_S^0$ selection	
Transverse momentum $p_T$	$> 0.2 \text{ GeV}/c$
$ \eta $	$< 0.8$
Invariant mass	$0.480 < m_{\pi^+\pi^-} < 0.515 \text{ GeV}/c^2$
DCA to primary vertex	$< 0.3 \text{ cm}$
Cosine of pointing angle	$> 0.9993$
Decay Length	$< 30 \text{ cm}$
$\pi^\pm$ Daughter Cuts	
$p_T$	$> 0.15 \text{ GeV}/c$
$ \eta $	$< 0.8$
DCA $\pi^+\pi^-$ Daughters	$< 0.3 \text{ cm}$
DCA to primary vertex	$> 0.3 \text{ cm}$
TPC and TOF $N_\sigma$ Cuts	
$p < 0.5 \text{ GeV}/c$	$N_{\sigma_{\text{TPC}}} < 3$
$p \geq 0.5 \text{ GeV}/c$	TOF & TPC available $N_{\sigma_{\text{TPC}}} < 3$
	$N_{\sigma_{\text{TOF}}} < 3$
	Only TPC available $N_{\sigma_{\text{TPC}}} < 3$

**Table 3:**  $K_S^0$  selection



(a)  $p\pi^-$  invariant mass distribution where the  $\Lambda$  peak is seen. (b)  $\pi^+\pi^-$  invariant mass distribution where the  $K_S^0$  peak is seen.

**Fig. 1:** (Color online) Invariant mass ( $m_{\text{inv}}$ ) distribution of  $p\pi^+$  pairs showing the  $\Lambda$  peak 1(a), and of  $\pi^+\pi^-$  pairs showing the  $K_S^0$  peak 1(b), for  $V^0$  candidates. The bottom panels are zoomed to show the background with fit. The vertical dashed lines represent the  $m_{\text{inv}}$  cuts used in the analyses, the vertical dotted lines delineate the region over which the background was fit, and the dash-dotted line shows the background fit.

The purpose of the average separation cut is to remove splitting and merging effects, and it is employed in the following way. The average separation between two tracks is calculated using their spatial separation as determined at several points throughout the TPC (every 20 cm radially from 85 cm to 245 cm). For the  $\Lambda K_S^0$  analysis, which involves two  $V^0$  particles, a minimum average separation cut of 6 cm between the like-charge daughters in the pairs is imposed (for example, between the p daughter of the  $\Lambda$  and the  $\pi^+$  daughter of the  $K_S^0$ ). For the  $\Lambda K^\pm$  analyses, a minimum average separation cut of 8 cm is enforced between the  $K^\pm$  and the  $\Lambda$  daughter sharing the same charge (for example, in the  $\Lambda K^+$  analysis, between the p daughter of the  $\Lambda$  and the  $K^+$ ). The cut values used coincide with the values at which the average separation correlation functions stabilize to unity, signifying the splitting and merging effects are no longer abundant. These effects between oppositely charged tracks were found to be negligible, therefore no cuts on unlike-charge tracks are imposed.

### 3 Analysis Methods

#### 3.1 Correlation Function

Two-particle correlation functions are built as the ratio of the covariant two-particle and single-particle spectra:

$$C^{ab}(\vec{p}_a, \vec{p}_b) = \frac{E_a E_b \frac{dN^{ab}}{d^3p_a d^3p_b}}{\left(E_a \frac{dN^a}{d^3p_a}\right) \left(E_b \frac{dN^b}{d^3p_b}\right)} \quad (1)$$

This may be expressed theoretically as in the Koonin-Pratt equation [16, 17]:

$$C(\mathbf{k}^*) = \int S_{\mathbf{P}}(\mathbf{r}^*) |\Psi_{\mathbf{k}^*}(\mathbf{r}^*)|^2 d^3\mathbf{r}^* \quad (2)$$

where  $\mathbf{k}^*$  is the relative momentum of the pair (defined as  $\mathbf{k}^* = \frac{1}{2}|\mathbf{p}_1^* - \mathbf{p}_2^*|$ , where  $\mathbf{p}_1^*$  and  $\mathbf{p}_2^*$  are the momenta of the two particles) in the pair rest frame (PRF),  $\mathbf{r}^*$  is the relative separation in the same frame,  $\mathbf{P}$  is the total pair momentum,  $S_{\mathbf{P}}(\mathbf{r}^*)$  is the pair source distribution, and  $\Psi_{\mathbf{k}^*}(\mathbf{r}^*)$  is the two-particle wave-function. Within the  $|\Psi|^2$  term is contained the particle interaction information, and therefore the scattering parameters.

In practice, the correlation function is formed experimentally as:

$$C(k^*) = \mathcal{N} \frac{A(k^*)}{B(k^*)} \quad (3)$$

where  $A(k^*)$  is the signal distribution,  $B(k^*)$  is the reference distribution, and  $\mathcal{N}$  is a normalization parameter.  $B(k^*)$  is used to divide out the phase-space effects, leaving only the femtoscopic effects in the correlation function. The normalization parameter is chosen such that the mean value of the correlation function equals unity for  $k^* \in [0.32, 0.4]$  GeV/c.

In practice,  $A(k^*)$  is constructed by binning in  $k^*$  pairs from the same event. Typically,  $B(k^*)$  is obtained using mixed-event pairs [18], i.e. particles from a given event are paired with those from another event. Other techniques exist; most notably, one may use same-event pairs after rotating one particle in the pair by  $180^\circ$  in the transverse plane (see Sec. 3.5 and App. A for more details). For this analysis, the typical mixed-event method is utilized, and each event is mixed with five others for the reference distribution construction. In order to mix only similar events, events are binned both in primary vertex location (2 cm bin width) and in centrality (5% bin width), and only events within a given bin are mixed; i.e. only events of like centrality and of like primary vertex location are mixed.

This analysis presents correlation functions for three centrality bins (0–10%, 10–30%, and 30–50%), and is pair transverse momentum ( $k_T = \frac{1}{2}|\mathbf{p}_{T,1} + \mathbf{p}_{T,2}|$ ) integrated (i.e. not binned in  $k_T$ ) due to limited statistics. The  $k_T$ -dependence of the three  $\Lambda K$  combinations is comparable, so an integrated analysis is acceptable. The correlation functions are constructed separately for the two magnetic field configurations ( $++$  and  $--$ ). These are kept separate during the fitting process, and are combined using a weighted average when plotting, where the weight is the number of numerator pairs in the normalization range.

### 3.2 Modeling the correlation function

In the absence of the Coulomb interaction, the correlation function can be described analytically with a model derived by Lednický and Lyuboshitz [5]. Within the model, the (non-symmetrized) two-particle wave function is expressed as a superposition of a plane wave and diverging spherical wave, and the complex scattering amplitude,  $f^S(k^*)$ , is evaluated via the effective range approximation

$$f^S(k^*) = \left( \frac{1}{f_0^S} + \frac{1}{2}d_0^S k^{*2} - ik^* \right)^{-1} \quad (4)$$

where  $f_0^S$  is the complex s-wave scattering length,  $d_0^S$  is the effective range of the interaction, and  $S$  denotes the total spin of the particular pair. A spherically symmetric Gaussian distribution with radius  $R_{\text{inv}}$  is assumed for the pair emission source in the PRF. With these assumptions, utilizing the Koonin-Pratt equation (Eq. 2), the correlation function for non-identical particle pairs with at least one uncharged member is given by [5]

$$C(k^*)_{\text{Lednický}} = 1 + \sum_S \rho_S \left[ \frac{1}{2} \left| \frac{f^S(k^*)}{R_{\text{inv}}} \right|^2 \left( 1 - \frac{d_0^S}{2\sqrt{\pi}R_{\text{inv}}} \right) + \frac{2\Re f^S(k^*)}{\sqrt{\pi}R_{\text{inv}}} F_1(2k^*R_{\text{inv}}) - \frac{\Im f^S(k^*)}{R_{\text{inv}}} F_2(2k^*R_{\text{inv}}) \right] \quad (5)$$

where  $\Re f^S(k^*)$  and  $\Im f^S(k^*)$  denote the real and imaginary parts of the complex scattering length, respectively, and  $F_1$  and  $F_2$  are the analytic functions. The weight factor,  $\rho_S$  is the normalized emission probability for a state of total spin  $S$ ; in the assumed case of unpolarized emission,  $\rho_S = (2S+1)/[(2j_1+1)(2j_2+1)]$ , where  $j_{1,2}$  are the spins of the particles in the pair. The  $\Lambda$  hyperon is spin-1/2 and K mesons are spin-0, so the  $\Lambda K$  system only has one possible total spin state  $S$ , and therefore  $C(k^*)$  in Eq. 5 has only a single term. In the following, the  $S$  superscript is dropped from all scattering parameters.



### 3.3 Residual Correlations

The purpose of this analysis is study the interaction and scale of the emitting source of the primary  $\Lambda K$  pairs. However, in practice some of the selected particles originate as decay products from other resonances, and some of the final pairs contain a misidentified member. In both cases, these contribute to the finally observed correlation function, and obscure its relation to the primary  $\Lambda K$  system. The contributions from fake pairs, which contain at least one misidentified member, are assumed to average to unity, in which case they simply attenuate the femtoscopic signal. Those pairs whose members originate as daughters from resonances carry information about the parent system. In effect, the correlation between the parents will be visible, although smeared out, in the daughters' signal. This is termed a residual correlation resulting from feed-down. As described in the following, the main sources of residual correlations in the  $\Lambda K$  systems result from  $\Lambda$  hyperons which have decayed from  $\Sigma^0$ ,  $\Xi^0$ , and  $\Xi^-$  parents.

The finally measured correlation function is a combination of the genuine  $\Lambda K$  correlation with contributions from resonances and impurities

$$C_{\text{measured}}(k_{\Lambda K}^*) = 1 + \lambda'_{\Lambda K} [C_{\Lambda K}(k_{\Lambda K}^*) - 1] + \sum_{ij} \lambda'_{ij} [C_{ij}(k_{\Lambda K}^*) - 1]$$

$$\lambda'_{ij} = \lambda_{\text{Fit}} \lambda_{ij}$$

$$\sum_{ij} \lambda'_{ij} = \lambda_{\text{Fit}} \sum_{ij} \lambda_{ij} = \lambda_{\text{Fit}} \quad (6)$$

where the  $\Lambda K$  term represents the genuine  $\Lambda K$  correlation, and the  $ij$  terms denote the contributions from residual feed-down and impurities. More specifically,  $C_{ij}(k_{\Lambda K}^*)$  is the correlation function of the parent system expressed in terms of the relative momentum of the daughter  $\Lambda K$  pair. The  $\lambda_{ij}$  parameters serve as weights dictating the relative strength of each component's contribution to the observed signal, and are normalized to unity (i.e.  $\sum_{ij} \lambda_{ij} = 1$ , where  $ij$  includes also the primary  $\Lambda K$  component). The individual  $\lambda_{ij}$  are fixed (and whose values can be found in Table 4), but the parameter  $\lambda_{\text{Fit}}$  in Eq. 6 is left free.

$\Lambda K^+$		$\bar{\Lambda} K^-$		$\Lambda K^-$		$\bar{\Lambda} K^+$	
Source	$\lambda$ value	Source	$\lambda$ value	Source	$\lambda$ value	Source	$\lambda$ value
Primary	0.527	Primary	0.526	Primary	0.526	Primary	0.527
$\Sigma^0 K^+$	0.111	$\bar{\Sigma}^0 K^-$	0.110	$\Sigma^0 K^-$	0.110	$\bar{\Sigma}^0 K^+$	0.111
$\Xi^0 K^+$	0.039	$\bar{\Xi}^0 K^-$	0.035	$\Xi^0 K^-$	0.038	$\bar{\Xi}^0 K^+$	0.036
$\Xi^- K^+$	0.050	$\bar{\Xi}^+ K^-$	0.046	$\Xi^- K^-$	0.050	$\bar{\Xi}^+ K^+$	0.046
Other	0.226	Other	0.235	Other	0.228	Other	0.233
Fakes	0.048	Fakes	0.048	Fakes	0.048	Fakes	0.048

$\Lambda K_S^0$		$\bar{\Lambda} K_S^0$	
Pair System	$\lambda$ value	Pair System	$\lambda$ value
Primary	0.543	Primary	0.544
$\Sigma^0 K_S^0$	0.120	$\bar{\Sigma}^0 K_S^0$	0.120
$\Xi^0 K_S^0$	0.042	$\bar{\Xi}^0 K_S^0$	0.039
$\Xi^- K_S^0$	0.054	$\bar{\Xi}^+ K_S^0$	0.050
Other	0.194	Other	0.199
Fakes	0.048	Fakes	0.048

**Table 4:**  $\lambda$  values for the individual components of the  $\Lambda K$  correlation functions.

To obtain the parent correlation function expressed in the relative momentum of the daughter pair, a transform matrix is utilized

$$C_{ij}(k_{\Lambda K}^*) \equiv \frac{\sum_{k_{ij}^*} C_{ij}(k_{ij}^*) T(k_{ij}^*, k_{\Lambda K}^*)}{\sum_{k_{ij}^*} T(k_{ij}^*, k_{\Lambda K}^*)} \quad (7)$$

where  $T(k_{ij}^*, k_{\Lambda K}^*)$  is the transform matrix, which is generated with the THERMINATOR 2 [19] simulation. The transform matrix describes the decay kinematics of the parent system into the daughter, and is essentially an unnormalized probability distribution mapping the  $k^*$  of the parent pair to that of the daughter pair when one or both parents decay (see Ref. [20] for more details).

In practice, the contribution of a parent system (e.g.  $\Sigma^0 K^+$ ) to the daughter correlation function (e.g.  $\Lambda K^+$ ) is determined by modeling the parent system's correlation function and running it through the appropriate transform matrix. Since the interactions between these particles are not known, all residual pairs are assumed to have the same source size as the daughter pair. Furthermore, Coulomb-neutral residual pairs are assumed to share the same scattering parameters as the daughter pair. When modeling  $\Xi^- K^\pm$  residual correlations, the experimental  $\Xi^- K^\pm$  data is used. Consistent results are found when modeling the  $\Xi^- K^\pm$  system, in which the the strong interaction is assumed to be negligible, and the parent correlation is generated assuming a Coulomb-only scenario (see Appendix B for more details). This approximation is well justified here as a Coulomb-only description of the system describes, reasonably well, the broad features of the correlation.

The  $\lambda_{ij}$  parameters dictate the relative strength of each contribution to the correlation function, and can be estimated using the THERMINATOR 2 and HIJING simulations. More specifically, the  $\lambda$  parameter for parent system  $ij$  is estimated as the total number of  $\Lambda K$  pairs in our experimental sample originating from  $ij$  ( $N_{ij}$ ) divided by the total number of  $\Lambda K$  pairs ( $N_{\text{Total}}$ ). The number of  $\Lambda K$  pairs involves both the raw yields and the reconstruction efficiencies. The reconstruction efficiencies ( $RE_{ij}$ ) are estimated with MC HIJING data, which has been run through GEANT to simulate the detector response. HIJING events are generated from a superposition of PYTHIA p-p collisions, and lack the strangeness saturation of a fully thermalized medium. As a result, HIJING is unreliable in providing the yields needed for this analysis, and, instead, the yields are estimated with the THERMINATOR 2 simulation ( $N_{ij}^{\text{THERM}}$ ). The number of  $\Lambda K$  pairs is then estimated as the product of the yield with the reconstruction efficiency,  $N_{ij} = N_{ij}^{\text{THERM}} RE_{ij}^{\text{HIJING}}$ .

Femtoscopic analyses are sensitive to the pair emission structure at kinetic freeze-out. Therefore, in the eyes of femtoscopy, any particle born from a resonance decay before last rescattering is seen as primary. The THERMINATOR 2 simulation shows that, aside from primaries, the  $\Lambda$  hyperons and  $K$  mesons decay from a large number of resonances ( $\sim 50$   $\Lambda$  parent species, and  $\sim 70$   $K$  parent species), and the most significant contributing pair systems are  $\Sigma^0 K$ ,  $\Xi^- K$ ,  $\Xi^0 K$ ,  $\Sigma^{*+} K$ ,  $\Sigma^{*-} K$ ,  $\Sigma^{*0} K$ ,  $\Lambda K^*$ ,  $\Sigma^0 K^*$ ,  $\Xi^- K^*$ , and  $\Xi^0 K^*$ . However, the simulation does not include a hadronic rescattering phase, and not all of the aforementioned pair systems will survive until kinetic freeze-out. The systems resulting from electromagnetic or weak decays ( $\Sigma^0$ ,  $\Xi^-$ , and  $\Xi^0$ ) will survive long after kinetic freeze-out, and will contribute residual signals to the  $\Lambda K$  correlation functions. The majority of the remaining contributors decay via the strong interaction with proper decay lengths less than a few fm, and whose daughters should always be considered primary. The proper decay length of the parent is used to judge whether or not the daughter is treated as primary. A decay product is considered primary if its parent has a mean proper lifetime  $\tau$  satisfying  $c\tau < 10$  fm. Changing  $c\tau$  only moderately affects the  $\lambda_{ij}$  parameters, and the effect is included the estimation of the systematic uncertainties. In order for a pair to be considered primary, both particles in the pair must be considered primary. If either parent has  $\tau > \tau_{\text{max}}$ , the daughter pair contributes to the “Other” category when calculating  $\lambda$  parameters. For this hodgepodge of pair systems, all with different two-particle interactions and single-particle source distributions, we assume the net correlation effect averages to unity. Residual contributions from  $\Sigma^0$ ,  $\Xi^0$ ,  $\Xi^-$  are accounted for in

the fit.

The  $\lambda$  values used can be found in Table 4, which also included values for “Other” and “Fakes”. The “Other” category contains pairs which are not considered primary, and which do not originate from the residual contributors accounted for in the fit. The “Fakes” category represents pairs that are mistakenly identified as ΛK. To estimate this  $\lambda_{\text{Fakes}}$  value, the number of fake pairs is assumed to be equal to the total number of simulated pairs multiplied by  $(1 - PP_{\Lambda K})/PP_{\Lambda K}$ , where  $PP_{\Lambda K}$  is the ΛK pair purity, estimated as the product of the two single-particle purities ( $PP_{\Lambda K} = P_{\Lambda}P_K$ ). More simply, this amounts to  $\lambda_{\text{Fakes}} = 1.0 - PP_{\Lambda K}$ . For both of these contributors (“Other” and “Fakes”), it is assumed that these correlations average to unity, and therefore do not contribute to the final correlation function.

### 3.4 Momentum Resolution Corrections

Finite track momentum resolution causes the reconstructed momentum of a particle to smear around the true value. This, of course, also holds true for  $V^0$  particles. The effect is propagated up to the pairs of interest, which causes the reconstructed relative momentum ( $k_{\text{Rec}}^*$ ) to differ from the true momentum ( $k_{\text{True}}^*$ ). The effects of finite momentum resolution are accounted for through the use of a response matrix generated with MC HIJING data. With this approach, the resolution correction is applied on-the-fly during the fitting process by propagating the theoretical (fit) correlation function through the response matrix, according to

$$C_{\text{fit}}(k_{\text{Rec}}^*) = \frac{\sum_{k_{\text{True}}^*} M_{k_{\text{Rec}}^*, k_{\text{True}}^*} C_{\text{fit}}(k_{\text{True}}^*)}{\sum_{k_{\text{True}}^*} M_{k_{\text{Rec}}^*, k_{\text{True}}^*}} \quad (8)$$

where  $M_{k_{\text{Rec}}^*, k_{\text{True}}^*}$  is the response matrix,  $C_{\text{fit}}(k_{\text{True}}^*)$  is the fit binned in  $k_{\text{True}}^*$ , and the denominator normalizes the result. Equation 8 describes that, for a given  $k_{\text{Rec}}^*$  bin, the observed value of  $C(k_{\text{Rec}}^*)$  is a weighted average of all  $C(k_{\text{True}}^*)$  values, where the weights are the normalized number of counts in the  $[k_{\text{Rec}}^*, k_{\text{True}}^*]$  bin.

### 3.5 Non-Femtoscopic Background

A significant non-femtoscopic background is observed in all of the studied ΛK correlations which increases with decreasing centrality, is the same amongst all  $\Lambda K^{\pm}$  pairs, and is more pronounced in the  $\Lambda K_S^0$  system (the difference in  $\Lambda K^{\pm}$  and  $\Lambda K_S^0$  backgrounds is due mainly to a difference in kinematic cuts). The background is due primarily to particle collimation associated with elliptic flow, and results from mixing events with unlike event-plane angles<sup>1</sup>[21]. The effect produces to the observed suppression at intermediate- $k^*$ , and should also lead to an enhancement at low- $k^*$ . The behavior of the non-femtoscopic background is needed in the low- $k^*$  signal region, but a clean view of it is only possible outside of such a region.

The THERMINATOR 2 simulation has been shown to reproduce the background features in a  $\pi K$  analysis [21]. The simulation does not include any final-state effects, but they can be introduced by weighting the numerator pairs with the modulus squared of the appropriate two-particle wave-function when building the signal distributions. For the present purpose, only the behavior of the non-femtoscopic background is desired, and unit weights are used. Figure 2 shows the THERMINATOR 2 simulation (open triangles) together with experimental data (closed circles). The figure also shows a 6<sup>th</sup>-order polynomial fit to the simulation (dashed curves), as well as the fit polynomial scaled to match the data (solid curves).

The description by THERMINATOR 2 of the non-femtoscopic backgrounds in the  $\Lambda K^{\pm}$  systems is remarkable, and can be used in a quantitative fashion to help fit the data. More specifically, the non-femtoscopic backgrounds were modeled by (6<sup>th</sup>-order) polynomial fits to THERMINATOR 2 simulation

<sup>1</sup> An attempt was made to decrease the background by binning events in  $\Psi_{\text{EP}}$ , but only a small reduction in the signal was achieved due to the limited event-plane resolution.

for the  $\Lambda K^\pm$  analyses; one polynomial for each centrality class. The form of each polynomial is set before use with the experimental data, by fitting to the THERMINATOR 2 simulation, shown in Fig. 2. The extracted polynomial is adjusted to best describe the data by introducing a scale factor and a vertical shift, both of which are determined by fitting to data in the region  $0.32 < k^* < 0.80$  GeV/c; during the fit of the low- $k^*$  signal region, the background is fixed. In all cases, the non-femtoscopic background correction was applied as a scale factor.

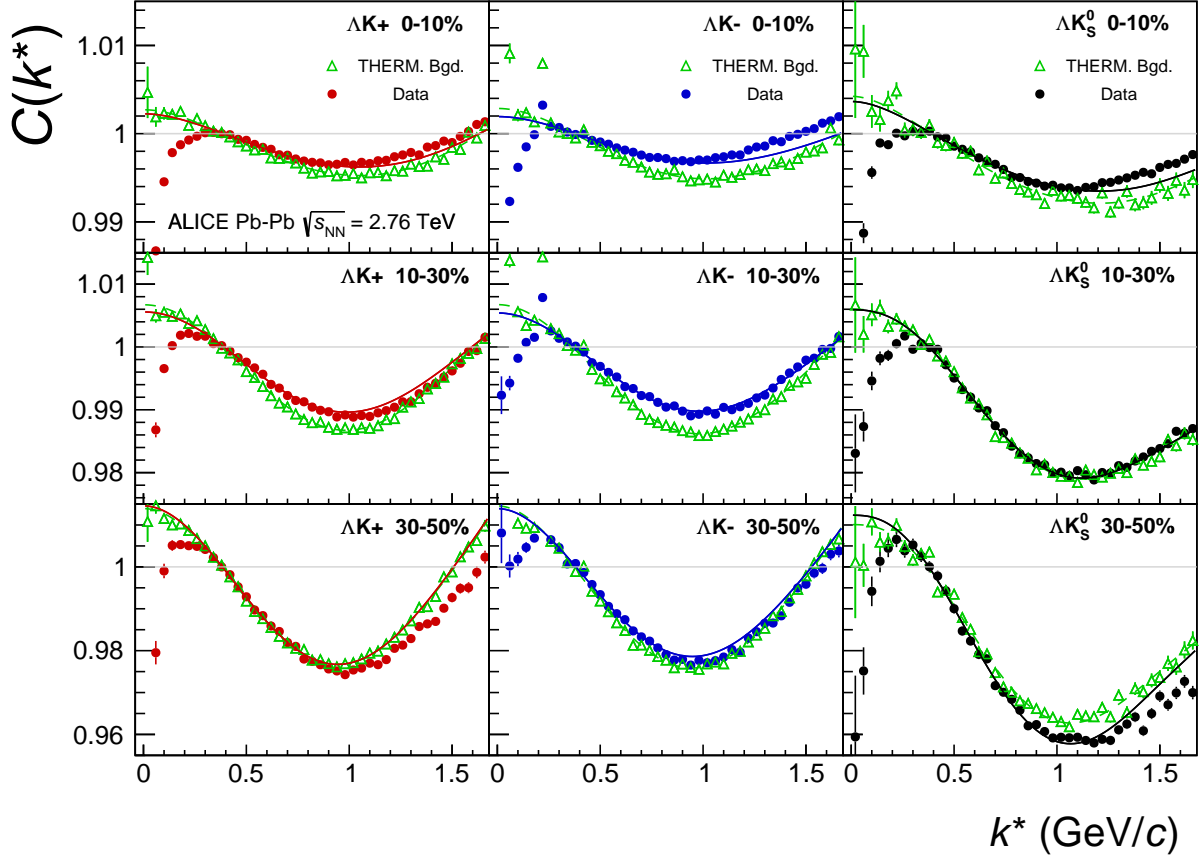


**Fig. 2:** (Color online) THERMINATOR 2 simulation (open triangles) together with experimental data (closed circles). Results are shown for  $\Lambda K^+$  (left),  $\Lambda K^-$  (middle), and  $\Lambda K_s^0$  (right). A 6<sup>th</sup>-order polynomial fit to the simulation is shown as a dashed curve. This polynomial is scaled to match the experimental data. The polynomial fit with scale factor applied is drawn as a solid curve.

An alternative approach to treating the non-femtoscopic background is to instead attempt to eliminate it. The background may be effectively reduced by forming the reference distribution ( $B(k^*)$ ) with the “Stavinskiy method”. With the Stavinskiy method, mixed-event pairs are not used for the reference distribution; instead, same-event pseudo-pairs, formed by rotating one particle in a real pair by  $180^\circ$  in the transverse plane, are used. This rotation rids the pairs of any femtoscopic correlation, while maintaining correlations due to elliptic flow (and other suitably symmetric contributors). The effect on the  $\Lambda K^+$  correlation functions can be seen in the appendix, in Fig. A.1.

### 3.6 Summarized correlation function construction

A simple  $\chi^2$  test is inappropriate for fitting correlation functions, as the ratio two Poisson distributions does not result in a Poisson distribution. Instead, a log-likelihood fit function is used as the statistic quantifying the quality of the fit [1]. The parameters included in the generation of a correlation function are:  $\lambda_{\text{Fit}}$ ,  $R$ ,  $f_0$  ( $\Re f_0$  and  $\Im f_0$  separately),  $d_0$ , and normalization  $N$ .

For the fit, a given pair and its conjugate (e.g.  $\Lambda K^+$  and  $\bar{\Lambda} K^-$ ) share scattering parameters ( $\Re f_0, \Im f_0, d_0$ ), and the three distinct analyses ( $\Lambda K^+$ ,  $\Lambda K^-$ , and  $\Lambda K_S^0$ ) are assumed to have scattering parameters unique from each other. The pair emission source for a given centrality class is assumed similar between all analyses; therefore, for each centrality, all  $\Lambda K$  analyses share a common radius parameter. For each centrality class, a single  $\lambda_{\text{Fit}}$  parameter (see Eq. 6) is shared amongst all. Finally, each correlation function has a unique normalization parameter.

All correlation functions are normalized in the range  $0.32 < k^* < 0.40$  GeV/c, and fit in the range  $0.0 < k^* < 0.30$  GeV/c. For the  $\Lambda K^-$  analysis, the region  $0.19 < k^* < 0.23$  GeV/c was excluded from the fit to exclude the bump caused by the  $\Omega^-$  resonance. For each pair system, contributions from three residual contributors are accounted for, as discussed in Sec. 3.3, and whose individual  $\lambda$  values are listed in Table 4. Effects of finite track momentum resolution are also accounted for, as outlined in Sec. 3.4. The non-femtoscopic backgrounds are modeled using the THERMINATOR 2 simulation, as described in Sec. 3.5.

To summarize, the complete fit function is constructed as follows. The uncorrected, primary, correlation function,  $C_{\Lambda K}(k_{\Lambda K, \text{True}}^*)$ , is constructed using Eq. 5. The correlation functions describing the parent systems which contribute residually,  $C_{ij}(k_{ij, \text{True}}^*)$ , are obtained using Eq. 5 for Coulomb-neutral pairs or experimental data for  $\Xi^- K^\pm$  contributions. The residual contributions are then found by running each parent correlation function through the appropriate transform matrix, via Eq. 7. The primary and residual correlations are combined, via Eq. 6 with Tab. 4, to form  $C'_{\text{Fit}}(k_{\text{True}}^*)$ . Corrections are applied to account for momentum resolution effects using Eq. 8, to obtain  $C'_{\text{Fit}}(k_{\text{Rec}}^*)$ . Finally, the non-femtoscopic background correction,  $F_{\text{Bgd}}(k_{\text{Rec}}^*)$  is applied and the final fit function is obtained,  $C_{\text{Fit}}(k_{\text{Rec}}^*) = \mathcal{N} \cdot C'_{\text{Fit}}(k_{\text{Rec}}^*) \cdot F_{\text{Bgd}}(k_{\text{Rec}}^*)$ , where  $\mathcal{N}$  is a normalization parameter.

### 3.7 Systematic uncertainties

To quantify the systematic errors on the data, all correlation functions built using all varied cut values were bin-by-bin averaged, and the resulting variance of each bin was taken as the systematic error. The cuts included in the systematic study, as well as the values used in the variations, are shown in Tab. ?? ( $\Lambda K_S^0$ ) and Tab. ?? ( $\Lambda K^\pm$ ). Note, the central value corresponds to that used in the analysis. Similarly, the fit parameters extracted from all of these correlation functions were averaged, and the resulting variances were taken as the systematic errors for the fit parameters. Additionally, for the extracted fit parameters, a systematic analysis was done on the fit method through varying the  $k^*$  fit range, as well as varying the modeling of the non-femtoscopic background. The choice of  $k^*$  fit range was varied by  $\pm 25\%$ . As previously stated, the non-femtoscopic backgrounds are modeled with a polynomial fit to the THERMINATOR 2 simulation, scaled to match the data. To study the contribution of this choice to our systematic errors, the backgrounds of all of the systems were modeled by fitting to the data with a linear, quadratic, and Gaussian form. The resulting uncertainties in the extracted parameter sets were combined with the uncertainties arising from the particle and pair cuts.

## 4 Results

Figures 3–5 show the  $\Lambda K$  data with fits for all studied centrality bins (0–10%, 10–30%, and 30–50%). All six  $\Lambda K$  systems ( $\Lambda K^+$ ,  $\bar{\Lambda} K^-$ ,  $\Lambda K^-$ ,  $\bar{\Lambda} K^+$ ,  $\Lambda K_S^0$ ,  $\bar{\Lambda} K_S^0$ ) are fit simultaneously across all centralities, with a single radius and normalization  $\lambda_{\text{Fit}}$  parameter for each centrality bin. Scattering parameters ( $\Re f_0, \Im f_0, d_0$ ) are shared between pair-conjugate systems, but assumed unique between the different  $\Lambda K$  charge combinations (i.e. a parameter set describing the  $\Lambda K^+$  &  $\bar{\Lambda} K^-$  system, a second set describing the  $\Lambda K^-$  &  $\bar{\Lambda} K^+$  system, and a third for the  $\Lambda K_S^0$  &  $\bar{\Lambda} K_S^0$  system). Each correlation function receives a unique normalization parameter. The fits are corrected for finite momentum resolution effects, non-femtoscopic backgrounds, and residual correlations resulting from the feed-down from resonances. In Figs. 3–5, lines represent statistical errors, while boxes represent systematic errors. The dotted curve shows the

$\Lambda K_S^0$ systematics	
DCA to PV $\Lambda$ ( $\bar{\Lambda}$ )	$< [0.4, 0.5, 0.6]$ cm
DCA to PV $K_S^0$	$< [0.2, 0.3, 0.4]$ cm
DCA $\Lambda$ ( $\bar{\Lambda}$ ) Daughters	$< [0.3, 0.4, 0.5]$ cm
DCA $K_S^0$ Daughters	$< [0.2, 0.3, 0.4]$ cm
$\cos(\theta_{PA})$ $\Lambda$ ( $\bar{\Lambda}$ ) to PV	$> [0.9992, 0.9993, 0.9994]$
$\cos(\theta_{PA})$ $K_S^0$ to PV	$> [0.9992, 0.9993, 0.9994]$
DCA to PV of p ( $\bar{p}$ ) Daughter of $\Lambda$ ( $\bar{\Lambda}$ )	$> [0.05, 0.1, 0.2]$ cm
DCA to PV of $\pi^-$ ( $\pi^+$ ) Daughter of $\Lambda$ ( $\bar{\Lambda}$ )	$> [0.2, 0.3, 0.4]$ cm
DCA to PV of $\pi^+$ Daughter of $K_S^0$	$> [0.2, 0.3, 0.4]$ cm
DCA to PV of $\pi^-$ Daughter of $K_S^0$	$> [0.2, 0.3, 0.4]$ cm
$\overline{\Delta r}$ of Like-Charge Daughters	$> [5, 6, 7]$ cm
$\Lambda K^\pm$ systematics	
DCA $\Lambda$ ( $\bar{\Lambda}$ ) to PV	$< [0.4, 0.5, 0.6]$ cm
DCA $\Lambda$ ( $\bar{\Lambda}$ ) Daughters	$< [0.3, 0.4, 0.5]$ cm
$\cos(\theta_{PA})$ $\Lambda$ ( $\bar{\Lambda}$ ) to PV	$> [0.9992, 0.9993, 0.9994]$
DCA to PV of p ( $\bar{p}$ ) Daughter of $\Lambda$ ( $\bar{\Lambda}$ )	$> [0.05, 0.1, 0.2]$ cm
DCA to PV of $\pi^-$ ( $\pi^+$ ) Daughter of $\Lambda$ ( $\bar{\Lambda}$ )	$> [0.2, 0.3, 0.4]$ cm
$\overline{\Delta r}$ of $\Lambda$ ( $\bar{\Lambda}$ ) Daughter with Same Charge as $K^\pm$	$> [7, 8, 9]$ cm
DCA to PV in Transverse Plane of $K^\pm$	$< [1.92, 2.4, 2.88]$ cm
DCA to PV in Longitudinal Direction of $K^\pm$	$< [2.4, 3.0, 3.6]$ cm

**Table 5:**  $\Lambda$ K systematics. In the table, the shorthand used is as follows:  $PA$  = pointing angle; PV = primary vertex; DCA = distance of closest approach;  $\overline{\Delta r}$  = average separation

primary ( $\Lambda K$ ) contribution to the fit (i.e.  $1 + \lambda'_{\Lambda K} C_{\Lambda K}(k_{\Lambda K}^*)$  in Eq. 6), the dashed curve shows the fit to the non-femtoscopic background, and the solid curve shows the final fit after all corrections have been applied.

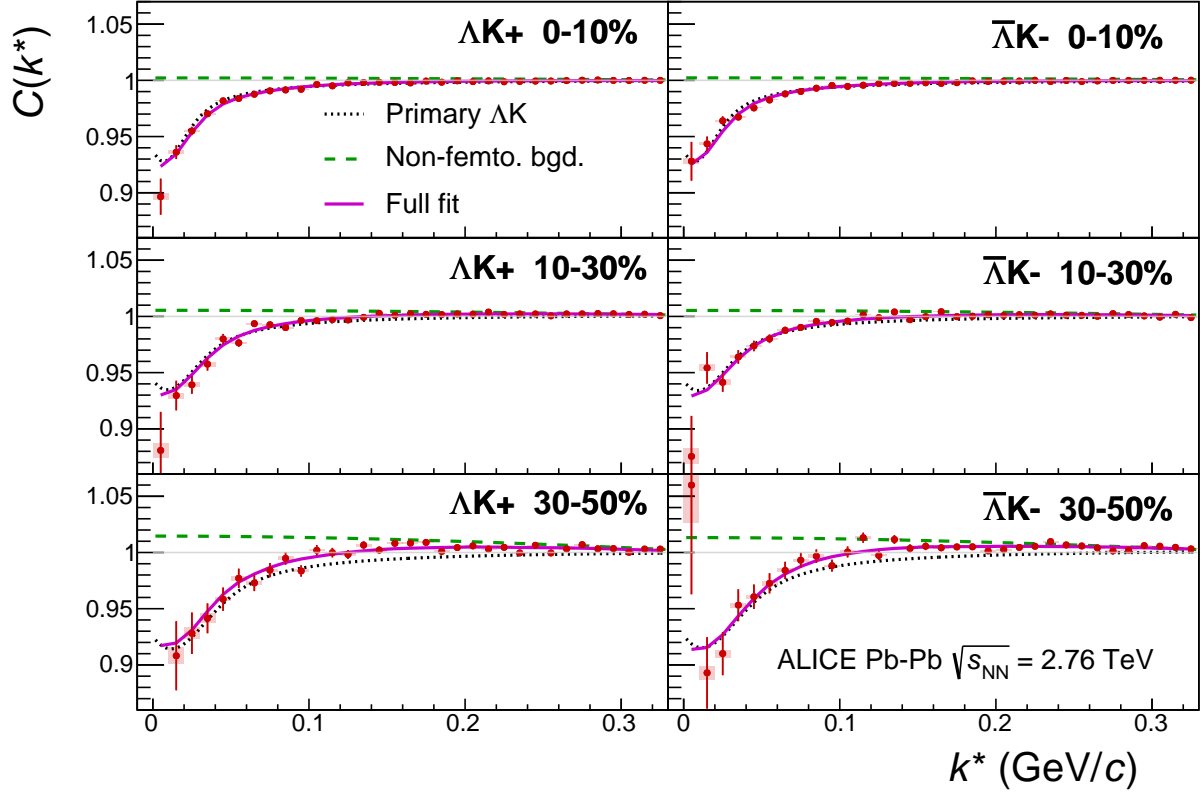


**Fig. 3:** (Color online) Fit results for the  $\Lambda K^+$  and  $\bar{\Lambda} K^-$  data. The  $\Lambda K^+$  data is shown in the left column, the  $\bar{\Lambda} K^-$  in the right, and the rows differentiate the different centrality bins (0–10% in the top, 10–30% in the middle, and 30–50% in the bottom). See text for further details.

Figure 6 summarizes well the results of the present study. In the summary plot, the extracted scattering parameters are shown in the form of a  $\Im f_0$  vs  $\Re f_0$  plot, which includes the  $d_0$  values to the right side. Also shown are the  $\lambda$  vs. radius parameters for all three studied centrality bins. In addition to the results of this study, theoretical predictions made using chiral perturbation theory [22, 23] are shown. For all  $\Lambda K$  systems, positive imaginary parts of the scattering lengths,  $\Im(f_0)$ , are extracted. This is expected, as  $\Im(f_0)$  describes the inelastic scattering channels. More interestingly, the results show that the  $\Lambda K^+$  and  $\Lambda K^-$  systems differ in the sign of the real part,  $\Re(f_0)$ , of their scattering lengths, with a negative value for  $\Lambda K^+$  and positive value for  $\Lambda K^-$ . The  $\Re f_0$  extracted for the  $\Lambda K_S^0$  system is positive, and within errors of that of the  $\Lambda K^-$ . The real part of the scattering length describes the effect of the strong interaction, making the difference in these systems quite intriguing. A positive  $\Re(f_0)$  ( $\Lambda K^-$ ,  $\Lambda K_S^0$ ) signifies that the effect of the strong force is attractive, while a negative  $\Re(f_0)$  ( $\Lambda K^+$ ) signifies a repulsion. Past studies of kaon-proton scattering found the  $K^-p$  interaction to be attractive, and that of the  $K^+p$  to be repulsive [2–4]. With respect to the kaons, this is similar to the current finding of an attractive  $\Lambda-K^-$  interaction and a repulsive  $\Lambda-K^+$  interaction. This difference could be due to an effect arising from different quark-antiquark interactions between the pairs ( $s\bar{s}$  in  $\Lambda K^+$ ,  $u\bar{u}$  in  $\Lambda K^-$ ). A related explanation could be that the effect is due to the different net strangeness for each system.

A comparison of the extracted radii from this study to those of other systems measure by ALICE [24] is shown in Figure 7. The figure shows extracted  $R_{\text{inv}}$  vs.  $m_T$  for several centralities and for several different

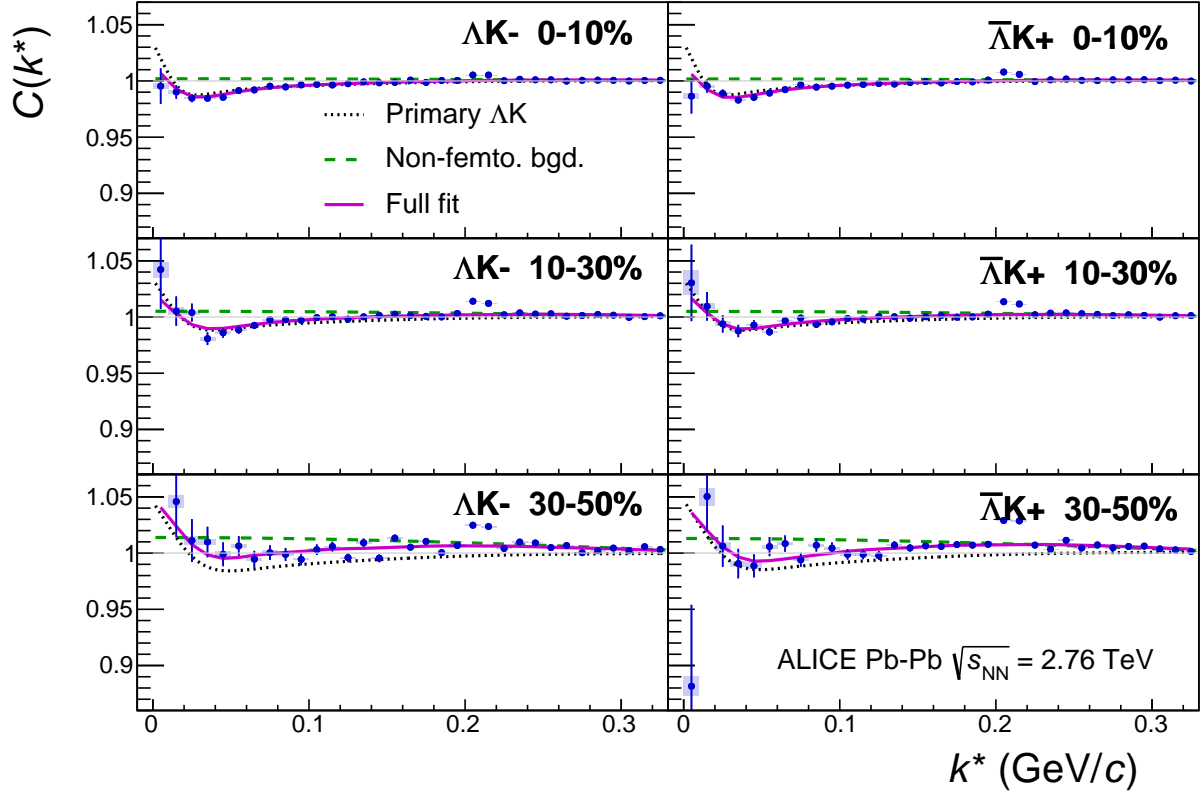


**Fig. 4:** (Color online) Fit results for the  $\Lambda K^-$  and  $\bar{\Lambda} K^+$  data. The  $\Lambda K^-$  data is shown in the left column, the  $\bar{\Lambda} K^+$  in the right, and the rows differentiate the different centrality bins (0–10% in the top, 10–30% in the middle, and 30–50% in the bottom). See text for further details.

systems. The  $m_T$  value used for the present  $\Lambda K$  results was taken as the average of the three systems<sup>1</sup>. The radii are observed to increase for more central events, as expected from a simple geometric picture of the collisions. They also demonstrate a decreasing size with increasing  $m_T$ , as expected in the presence of collective radial flow [25]. It was found that [26], even in the presence of good global  $m_T$ -scaling for the three-dimensional radii in the Longitudinally Co-Moving System (LCMS), a particle species dependence will exist for the  $R_{\text{inv}}$  measured in the Pair Rest Frame (PRF), due to trivial kinematic reasons. These kinematic effects, resulting from the transformation from LCMS to PRF, causes smaller masses to exhibit larger  $R_{\text{inv}}$  [24] (explaining, for instance, how the pion radii are systematically higher than kaon radii at the same approximate  $m_T$ ).

It is clear from the results in Fig. 7 that the  $\Lambda K$  systems do not conform to the approximate  $m_T$ -scaling of the identical particle pair source sizes. At first thought, this may appear to be a troubling result; the approximate scaling is an observed consequence of the collective behavior of the soft (low- $p_T$ ) sector of the produced system. The  $\Lambda$  and  $K$  particles certainly participate in the collective expansion of the QGP medium, but, importantly, they are non-identical particles, and all other systems in Fig. 7 contain identical particles. In the case of identical particle femtoscopy, the pair source is comprised of two

<sup>1</sup> For non-identical particle pairs, to be more directly analogous to the single particle  $m_T$ , the definition of the pair transverse mass used in this study is

$$\begin{aligned} m_{T,\text{pair}}^2 &= \left(\frac{m_{\text{inv}}}{2}\right)^2 + \left(\frac{1}{2}|\mathbf{p}_{T,1} + \mathbf{p}_{T,2}|\right)^2 \\ &= (K^0)^2 - (K^3)^2 \\ \text{where } K^\mu &\equiv \frac{1}{2}(p_1^\mu + p_2^\mu) \end{aligned}$$



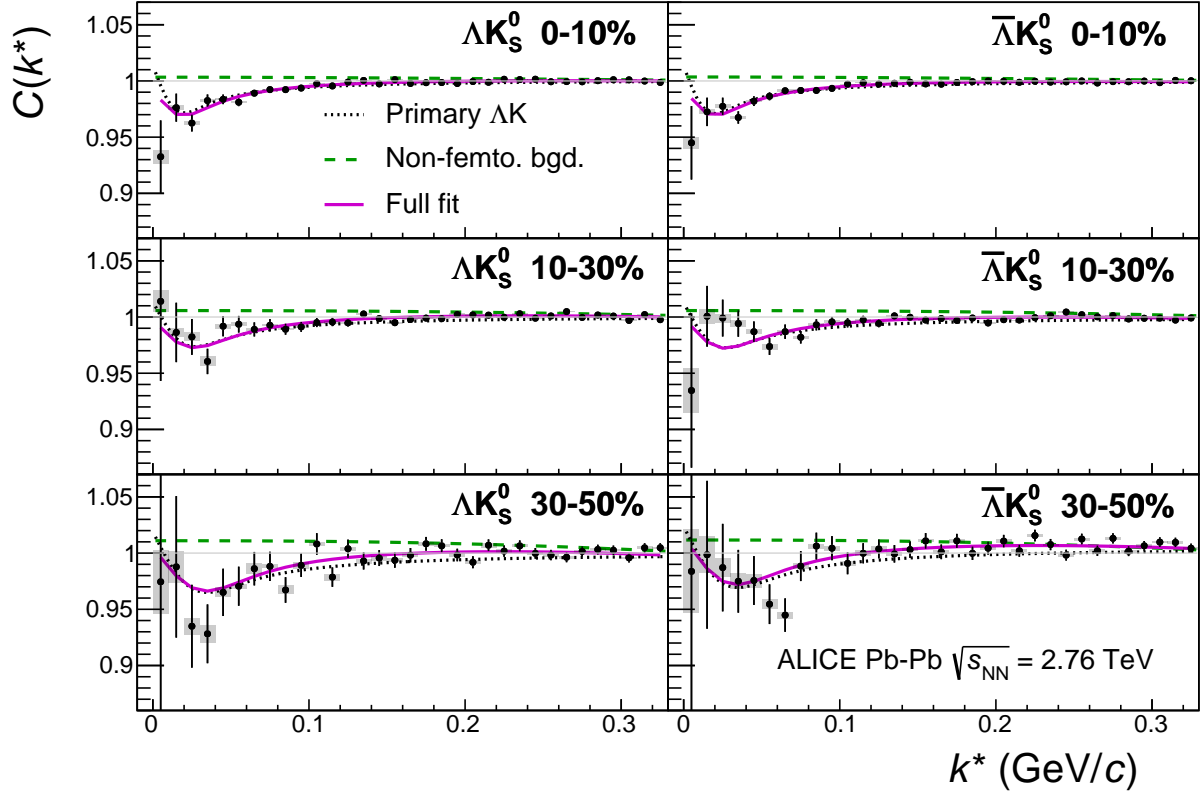


**Fig. 5:** (Color online) Fit results for the  $\Lambda K_S^0$  and  $\bar{\Lambda} K_S^0$  data. The  $\Lambda K_S^0$  data is shown in the left column, the  $\bar{\Lambda} K_S^0$  in the right, and the rows differentiate the different centrality bins (0–10% in the top, 10–30% in the middle, and 30–50% in the bottom). See text for further details.

identical single particle sources, and the pair source size extracted is simply a factor  $\sqrt{2}$  larger than those single particle sources. Thus, the identical particle pair source radii naturally follow the single particle source  $m_T$ -scaling in a simple manner.

When dealing with non-identical particles, the pair emission source, which is measured by femtoscopy, is the superposition of two single-particle sources. The hydrodynamic nature of the medium produces the approximate  $m_T$ -scaling with respect to these single-particle sources, not the pair sources. More specifically, the hydrodynamic response of the system confines higher- $m_T$  particles to smaller homogeneity regions, also pushes their average emission points further in the “out” direction [27]. Therefore, it is expected that the  $\Lambda$  source is both smaller in size and further out in the fireball than that of the kaons. The combination of two unique sources separated in space-time, when probing correlations between non-identical particle pairs, can lead to extracted radii falling outside of the (identical particle femtoscopy)  $m_T$ -scaling trend.

It is well established that non-identical particle femtoscopic studies are able to probe deeper than the second moments of the pair distribution functions accessed via identical particle studies. In addition to this, non-identical particle studies are able to measure the relative emission shifts, the first moments of the emission function [28]. For the study of  $\Lambda K$  pairs at mid-rapidity in Pb-Pb collisions, a separation of the single-particle sources in the out direction is expected. One elegant method for extracting information about the emission asymmetries is via a spherical decomposition of the correlation function. With this method, one can draw a wealth of information from just a few components of the decomposition. Particularly, the  $C_{00}$  component is similar to the 1D correlation functions typically studied, and probes the overall size of the source. The  $\Re C_{11}$  component probes the asymmetry of the system in the out direction; a non-zero value reveals the asymmetry.

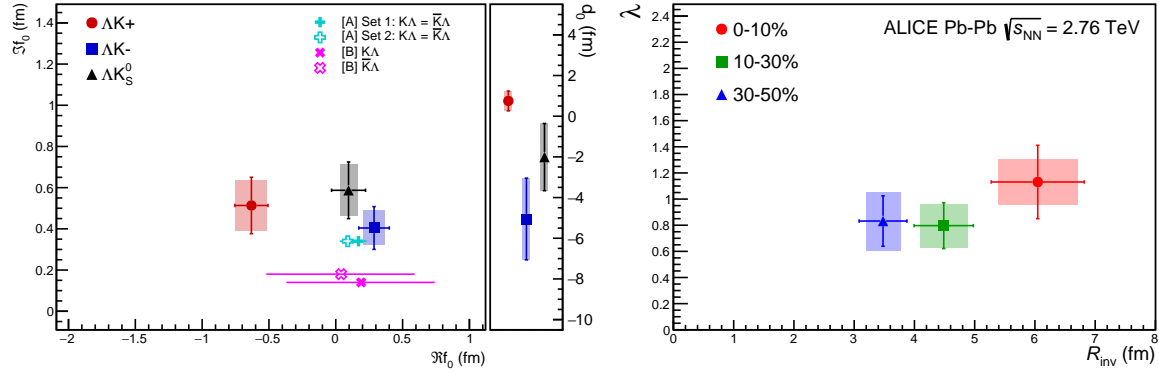


**Fig. 6:** (Color online) Extracted fit parameters for all of the  $\Lambda$ K systems. [Left]:  $\Im f_0$  vs.  $\Re f_0$ , together with  $d_0$  to the right for the  $\Lambda K^+$  (circles),  $\Lambda K^-$  (squares) and  $\Lambda K_S^0$  (triangles) systems. [Right]:  $\lambda$  vs. Radius for the 0–10% (circles), 10–30% (squares), and 30–50% (triangles) centrality bins. In the fit, all  $\Lambda$ K systems share common radii. The cross ([A] = Ref. [22]) and X symbols ([B] = Ref. [23]) points show theoretical predictions made using chiral perturbation theory.

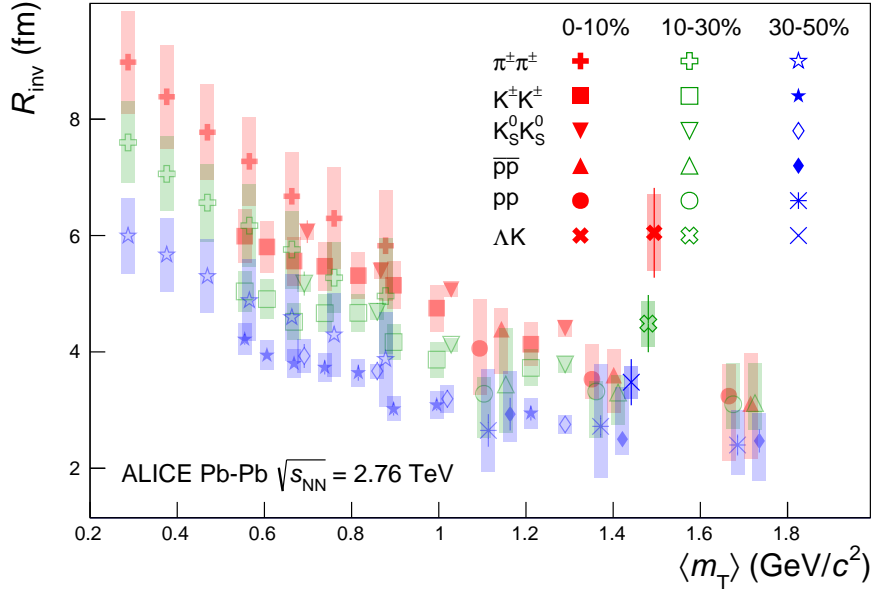


**Fig. 7:** (Color online) Extracted fit  $R_{\text{inv}}$  parameters as a function of pair transverse mass ( $m_T$ ) for various pair systems over several centralities. The ALICE published data [24] is shown with transparent, open symbols.

Figure 8 shows the  $C_{00}$  and  $\Re C_{11}$  components from the spherical decomposition of the  $\Lambda K^+$  data in the 0–10% centrality bin. The  $\Re C_{11}$  component shows a clear deviation from zero, and the negative value signifies that the  $\Lambda$  particles are, on average, emitted further out and/or earlier than the K mesons. This effect is supported by the results obtained from the THERMINATOR 2 model, shown in Fig. C.1. The effect of a non-zero shift in the source will naturally lead to larger measured radii. This is intuitive, and also reaffirmed in the simulation with THERMINATOR 2 shown in App. C. Larger effective radii are also found to result from inserting a Gaussian source with a non-zero shift into the Koonin-Pratt equation and numerically integrating.

It should be emphasized that the extracted  $\Lambda$ K source sizes do not indicate any sort of contradiction with the hydrodynamic nature of the system dictating the substructure of the femtoscopic radii. The results, rather, support this picture. As described above, the hydrodynamic response of the system confines

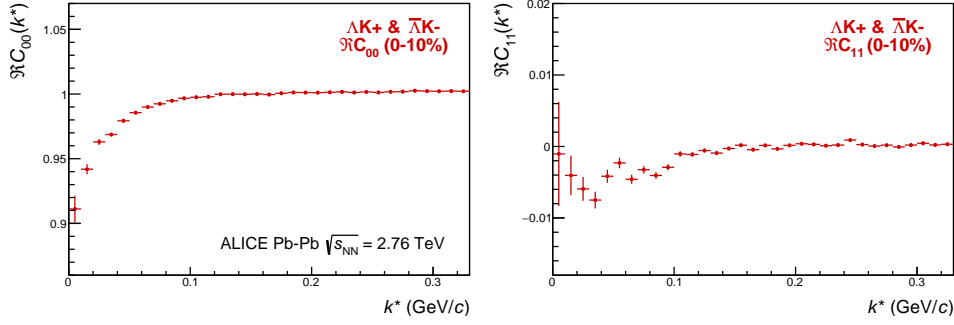


**Fig. 8:** (Color online)  $C_{00}$  (left) and  $\Re C_{11}$  (right) components of a spherical harmonic decomposition of the  $\Lambda K^+$  correlation function for the 0–10% centrality bin. The  $C_{00}$  component is similar to the 1D correlation functions typically studied, and probes the overall size of the source. The  $\Re C_{11}$  component probes the asymmetry in the system; a non-zero value reveals the asymmetry

the  $\Lambda$  emission to smaller homogeneity regions located further out in the fireball, as compared to the kaons. Therefore, the single particle  $\Lambda$  and  $K$  source sizes differ both in size and space-time location. When studying these pairs under the assumption of a spherically symmetric Gaussian source with no offset in the “out” direction, this can lead to larger extracted radii, as demonstrated above with the THERMINATOR 2 simulation.

## 5 Summary

Results from a femtoscopic analysis of  $\Lambda K$  correlations in Pb-Pb collisions at  $\sqrt{s_{NN}} = 2.76$  TeV with ALICE at the LHC have been presented. The femtoscopic radii,  $\lambda$  parameters, and scattering parameters were extracted from one-dimensional correlation functions in terms of the invariant momentum difference. The scattering parameters of  $\Lambda K$  pairs in all three charge combinations ( $\Lambda K^+$ ,  $\Lambda K^-$ , and  $\Lambda K_S^0$ ) have been measured for the first time. A striking difference in the  $\Lambda K^+$  and  $\Lambda K^-$  correlation functions is observed, which is reflected in the unique set of scattering parameters extracted for each. The  $\Lambda K_S^0$  systems is somewhat intermediate to these two cases. The  $\Lambda K^+$  systems exhibits a negative  $\Re(f_0)$ , while those extracted from the  $\Lambda K^-$  and  $\Lambda K_S^0$  systems are positive. This implies that the strong interaction is repulsive for the  $\Lambda K^+$  system and attractive for  $\Lambda K^-$  and  $\Lambda K_S^0$ . The physics underlying this phenomenon is currently not well understood, but this could be due to different quark-antiquark interactions between the pairs, or from different net strangeness for each system. The non-femtoscopic background is found to result almost entirely from collective effects, and is described quantitatively with unprecedented precision with the THERMINATOR 2 event generator. Finally, the  $\Lambda K$  systems exhibit source radii larger than expected from extrapolation from identical particle femtoscopic studies. This effect is interpreted as resulting from the separation in space-time of the single-particle  $\Lambda$  and  $K$  source distributions.

## Acknowledgements

## References

- [1] M. A. Lisa, S. Pratt, R. Soltz, and U. Wiedemann, “Femtoscopy in relativistic heavy ion collisions,” *Ann. Rev. Nucl. Part. Sci.* **55** (2005) 357–402, arXiv:nuc1-ex/0505014 [nuc1-ex].
- [2] W. E. Humphrey and R. R. Ross, “Low-Energy Interactions of  $K^-$  Mesons in Hydrogen,” *Phys. Rev.* **127** (1962) 1305–1323.
- [3] D. Hadjimichef, J. Haidenbauer, and G. Krein, “Short range repulsion and isospin dependence in the  $KN$  system,” *Phys. Rev.* **C66** (2002) 055214, arXiv:nuc1-th/0209026 [nuc1-th].

- [4] Y. Ikeda, T. Hyodo, and W. Weise, “Chiral SU(3) theory of antikaon-nucleon interactions with improved threshold constraints,” *Nucl. Phys.* **A881** (2012) 98–114, arXiv:1201.6549 [nucl-th].
- [5] R. Lednický and V. L. Lyuboshitz, “Final State Interaction Effect on Pairing Correlations Between Particles with Small Relative Momenta,” *Sov. J. Nucl. Phys.* **35** (1982) 770. [Yad. Fiz.35,1316(1981)].
- [6] ALICE Collaboration, K. Aamodt *et al.*, “The alice experiment at the cern lhc,” *JINST* **3** (2008) S08002. <http://stacks.iop.org/1748-0221/3/i=08/a=S08002>.
- [7] ALICE Collaboration, B. Abelev *et al.*, “Centrality determination of Pb-Pb collisions at  $\sqrt{s_{NN}} = 2.76$  TeV with ALICE,” *Phys. Rev.* **C88** no. 4, (2013) 044909, arXiv:1301.4361 [nucl-ex].
- [8] J. Alme *et al.*, “The ALICE TPC, a large 3-dimensional tracking device with fast readout for ultra-high multiplicity events,” *Nucl. Instrum. Meth. A* **622** (2010) 316–367, arXiv:1001.1950 [physics.ins-det].
- [9] B. A. et al and T. A. Collaboration, “Technical Design Report for the Upgrade of the ALICE Inner Tracking System,” *Journal of Physics G: Nuclear and Particle Physics* **41** no. 8, (2014) 087002. <http://stacks.iop.org/0954-3899/41/i=8/a=087002>.
- [10] ALICE Collaboration, B. B. Abelev *et al.*, “Performance of the ALICE Experiment at the CERN LHC,” *Int. J. Mod. Phys.* **A29** (2014) 1430044, arXiv:1402.4476 [nucl-ex].
- [11] A. Akindinov *et al.*, “Performance of the ALICE Time-Of-Flight detector at the LHC,” *Eur. Phys. J. Plus* **128** (2013) 44.
- [12] X.-N. Wang and M. Gyulassy, “HIJING: A Monte Carlo model for multiple jet production in pp, pA, and AA collisions,” *Phys. Rev. D* **44** (Dec, 1991) 3501–3516. <https://link.aps.org/doi/10.1103/PhysRevD.44.3501>.
- [13] R. Brun, F. Bruyant, F. Carminati, S. Giani, M. Maire, A. McPherson, G. Patrick, and L. Urban, “GEANT Detector Description and Simulation Tool,”.
- [14] ALICE Collaboration, S. Acharya *et al.*, “Kaon femtoscopy in Pb-Pb collisions at  $\sqrt{s_{NN}} = 2.76$  TeV,” *Phys. Rev.* **C96** no. 6, (2017) 064613, arXiv:1709.01731 [nucl-ex].
- [15] Particle Data Group Collaboration, C. Patrignani *et al.*, “Review of Particle Physics,” *Chin. Phys.* **C40** no. 10, (2016) 100001.
- [16] S. E. Koonin, “Proton Pictures of High-Energy Nuclear Collisions,” *Phys. Lett.* **B70** (1977) 43–47.
- [17] S. Pratt, T. Csorgo, and J. Zimanyi, “Detailed predictions for two pion correlations in ultrarelativistic heavy ion collisions,” *Phys. Rev.* **C42** (1990) 2646–2652.
- [18] G. I. Kopylov, “Like particle correlations as a tool to study the multiple production mechanism,” *Phys. Lett.* **B50** (1974) 472–474. [,39(1974)].
- [19] M. Chojnacki, A. Kisiel, W. Florkowski, and W. Broniowski, “THERMINATOR 2: THERMal heavy IoN generATOR 2,” *Comput. Phys. Commun.* **183** (2012) 746–773, arXiv:1102.0273 [nucl-th].
- [20] A. Kisiel, H. Zbroszczyk, and M. Szymaski, “Extracting baryon-antibaryon strong interaction potentials from pA femtoscopic correlation functions,” *Phys. Rev.* **C89** no. 5, (2014) 054916, arXiv:1403.0433 [nucl-th].

- [21] A. Kisiel, “Non-identical particle correlation analysis in the presence of non-femtoscopic correlations,” *Acta Physica Polonica B* **48** (04, 2017) 717.
- [22] Y.-R. Liu and S.-L. Zhu, “Meson-baryon scattering lengths in HB  $\chi$  PT,” *Phys. Rev.* **D75** (2007) 034003, arXiv:hep-ph/0607100 [hep-ph].
- [23] M. Mai, P. C. Bruns, B. Kubis, and U.-G. Meissner, “Aspects of meson-baryon scattering in three and two-flavor chiral perturbation theory,” *Phys. Rev.* **D80** (2009) 094006, arXiv:0905.2810 [hep-ph].
- [24] ALICE Collaboration, J. Adam *et al.*, “One-dimensional pion, kaon, and proton femtoscopy in Pb-Pb collisions at  $\sqrt{s_{NN}}=2.76$  TeV,” *Phys. Rev.* **C92** no. 5, (2015) 054908, arXiv:1506.07884 [nucl-ex].
- [25] S. V. Akkelin and Yu. M. Sinyukov, “The HBT interferometry of expanding sources,” *Phys. Lett.* **B356** (1995) 525–530.
- [26] A. Kisiel, M. Gaayn, and P. Boek, “Pion, kaon, and proton femtoscopy in Pb–Pb collisions at  $\sqrt{s_{NN}}=2.76$  TeV modeled in (3+1)D hydrodynamics,” *Phys. Rev.* **C90** no. 6, (2014) 064914, arXiv:1409.4571 [nucl-th].
- [27] F. Retiere and M. A. Lisa, “Observable implications of geometrical and dynamical aspects of freeze out in heavy ion collisions,” *Phys. Rev.* **C70** (2004) 044907, arXiv:nucl-th/0312024 [nucl-th].
- [28] A. Kisiel, “Non-identical particle femtoscopy at  $\sqrt{s_{NN}} = 200$  GeV in hydrodynamics with statistical hadronization,” *Phys. Rev.* **C81** (2010) 064906, arXiv:0909.5349 [nucl-th].
- [29] A. Stavinskiy *et al.*, “Some new aspects of femtoscopy at high energy,” *Nukleonika* **49** (Supplement 2) (2004) S23.
- [30] R. Lednický, “Finite-size effects on two-particle production in continuous and discrete spectrum,” *Phys. Part. Nucl.* **40** (2009) 307–352, arXiv:nucl-th/0501065 [nucl-th].

## A Stavinskiy Reference Method

Another option for obtaining the reference distribution,  $B(k^*)$ , is to use, what will be referred to as, the “Stavinskiy method” [29]. The method was first proposed to handle the case of one event femtoscopy, and has been suggested for use in eliminating momentum conservation effects in the reference distribution [1]. The method is appropriate for collisions between symmetric projectiles, at sufficiently large energy, with a detector which is symmetrical with respect to the transition  $\mathbf{r} \rightarrow -\mathbf{r}$ . The purpose of using the Stavinskiy method in this ΛK analysis is to rid the correlation functions of the non-femtoscopic background. More specifically, the intent is to handle background contributions from elliptic flow, and other sources having reflection symmetry in the transverse plane. With the Stavinskiy method, mixed-event pairs are not used for the reference distribution; instead, same-event pseudo-pairs, formed by rotating one particle in a real pair by  $180^\circ$  in the transverse plane, are used. This rotation rids the pairs of any femtoscopic correlation, while maintaining correlations due to elliptic flow (and other suitably symmetric contributors). The results of correctly implementing such a procedure are shown in Figure A.1. The figure shows the Stavinskiy method does a very good job of ridding the  $\Lambda K^+$  correlations of their non-femtoscopic backgrounds.

Now, one must be somewhat careful when applying this Stavinskiy method. To obtain correct results, the pseudo-pairs must be run through the same pair cuts used for the real pairs in the analyses. In an ideal world, the pair cut would only remove truly bad pairs results from splitting, merging, etc. In the real world, the pair cut always throws out some of the good with the bad. For the pseudo-pairs to form a reliable reference, they too must experience the pair cut, and the loss of “good” pseudo-pairs. This issue affected mainly the  $\Lambda K^+$  &  $\bar{\Lambda} K^-$  system in this analysis.

## B Strong and Coulomb Fitter

When modeling systems which include both strong and Coulomb effects, Eq. 5 is no longer valid, and, in fact, there is no analytical form with which to fit. To solve such a problem, and to fit such a system, one must develop a more fundamental model, beginning with Eq. 2 and using the two-particle wave-function including both strong and Coulomb interactions [30]:

$$\Psi_{\mathbf{k}^*}(\mathbf{r}^*) = e^{i\delta_c} \sqrt{A_c(\eta)} [e^{i\mathbf{k}^* \cdot \mathbf{r}^*} F(-i\eta, 1, i\xi) + f_c(k^*) \frac{\tilde{G}(\rho, \eta)}{r^*}] \quad (\text{B.1})$$

where  $\rho = k^* r^*$ ,  $\eta = (k^* a_c)^{-1}$ ,  $\xi = \mathbf{k}^* \cdot \mathbf{r}^* + k^* r^* \equiv \rho(1 + \cos \theta^*)$ , and  $a_c = (\mu z_1 z_2 e^2)^{-1}$  is the two-particle Bohr radius (including the sign of the interaction).  $\delta_c$  is the Coulomb s-wave phase shift,  $A_c(\eta)$  is the Coulomb penetration factor,  $\tilde{G} = \sqrt{A_c}(G_0 + iF_0)$  is a combination of the regular ( $F_0$ ) and singular ( $G_0$ ) s-wave Coulomb functions.  $f_c(k^*)$  is the s-wave scattering amplitude

$$f_c(k^*) = \left[ \frac{1}{f_0} + \frac{1}{2} d_0 k^{*2} - \frac{2}{a_c} h(\eta) - i k^* A_c(\eta) \right]^{-1} \quad (\text{B.2})$$

where, the “h-function”,  $h(\eta)$ , is expressed through the digamma function,  $\psi(z) = \Gamma'(z)/\Gamma(z)$  as

$$h(\eta) = 0.5[\psi(i\eta) + \psi(-i\eta) - \ln(\eta^2)] \quad (\text{B.3})$$

In this case, the  $\lambda$  parameter may be included as:

$$C(\mathbf{k}^*) = (1 - \lambda) + \lambda \int S(\mathbf{r}^*) |\Psi_{\mathbf{k}^*}^S(\mathbf{r}^*)|^2 d^3 \mathbf{r}^* \quad (\text{B.4})$$

To build a fit function for a system including both strong and Coulomb interactions two related options were considered. The first option was to numerically integrate Eq. 2. The second option was to simulate

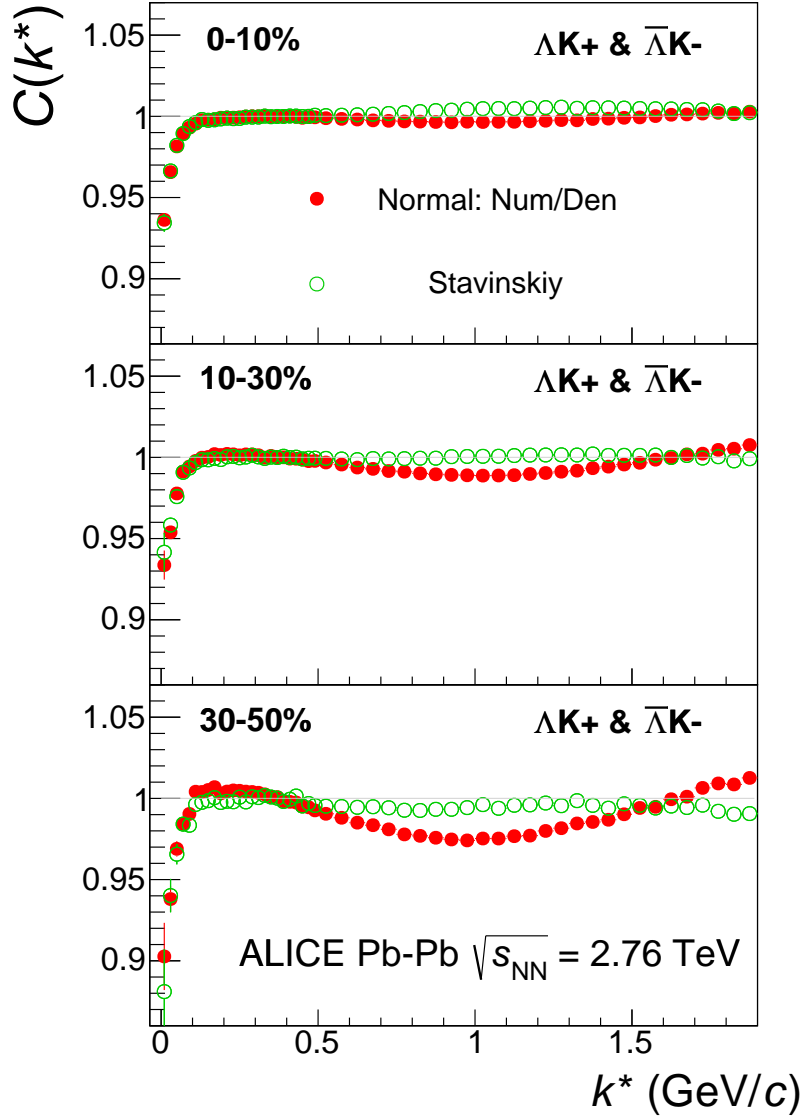


**Fig. A.1:** (Color online)  $\Lambda K^+ (\bar{\Lambda} K^-)$  correlation functions built using the Stavinskiy method for 0–10%, 10–30%, and 30–50% centralities. Closed symbols represent correlations built using the normal mixed-event reference distribution, while open symbols represent correlations formed using the Stavinskiy same-event pseudo-pairs as a reference.

a large sample of particle pairs, calculate the wave function describing the interaction, and average to obtain the integral in Eq. 2. In either case, the solution would involve some very complicated mathematical functions, as can be seen in Eqs. B.1 to B.3. Having no experience with either of these options, we elected the latter of simulating pairs.

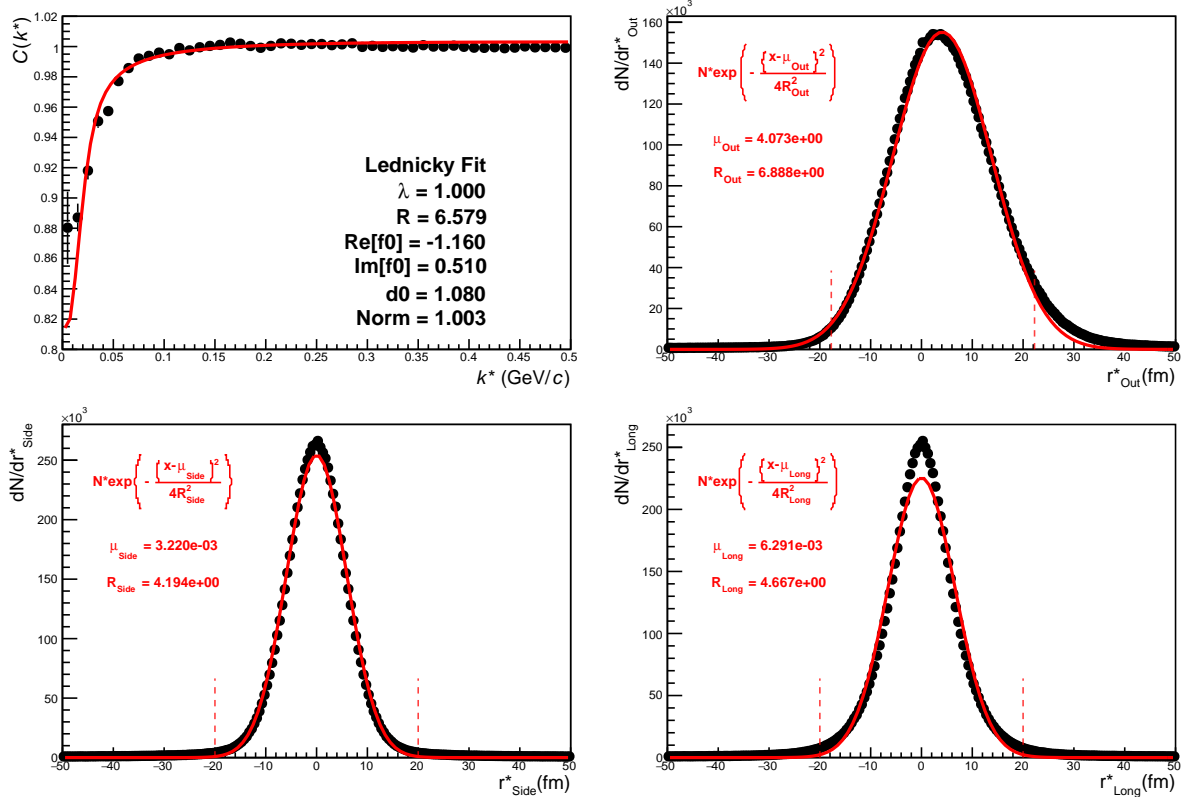
## C Relative Emission Shifts with THERMINATOR 2

Fig. C.1 shows results from the THERMINATOR 2 event generator for an impact parameter of  $b = 2$  fm. As THERMINATOR 2 does not include any final state effects, the femtoscopic correlation was introduced by assuming a set of scattering parameters  $(\Re f_0, \Im f_0, d_0) = (-1.16, 0.51, 1.08)$  and weighting the signal distribution (numerator pairs) with the modulus squared of the two-particle wave function,  $|\Psi|^2$ .

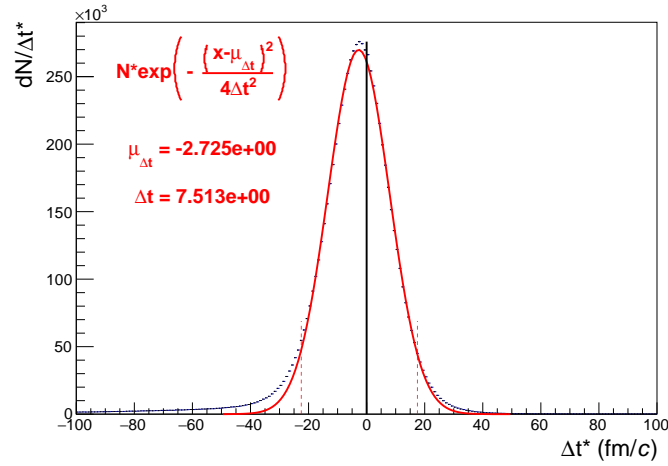
The top left of Fig. C.1(a) shows a fit to the one-dimensional correlation function from THERMINATOR 2. The scattering parameters are known precisely here, as they served as the weights used in the simulation, and are kept constant in the fit. Only the extracted one-dimensional source size is of interest here, so the  $\lambda$  parameter is also fixed at unity. The other three plots in Fig. C.1(a) show the source distribution in the out (top right), side (bottom left), and long (bottom right) directions (all in the PRF). The source distributions have all been fitted with a Gaussian form, the result of which is printed within the respective plot. One immediately sees a significant shift in the out direction,  $\mu_{\text{out}} \approx 4$  fm, and negligible shift in the other two directions,  $\mu_{\text{side}} \approx \mu_{\text{long}} \approx 0$  fm. The figure demonstrates that, within the THERMINATOR 2 model, the  $\Lambda$  is, on average, emitted further out than its K partner. Finally, Fig. C.1(b) shows the distribution of the relative time of emittance, again in the PRF. The figure shows that the  $\Lambda$  is, on average, emitted earlier than its K partner.

This section concludes with a brief look at how a spatial separation of the single particle sources affects the radii extracted from a femtoscopic analysis. To achieve this, THERMINATOR 2 is used in a similar fashion as described above, but with one important difference. Instead of taking the source information from THERMINATOR 2, the source is drawn from a pre-determined Gaussian distribution. In all cases,  $R_{\text{out}} = R_{\text{side}} = R_{\text{long}} = 5$  fm, and  $\mu_{\text{side}} = \mu_{\text{long}} = 0$  fm. In Figure C.2, results are shown for the case of  $\mu_{\text{out}} = 1$  fm,  $\mu_{\text{out}} = 3$  fm, and  $\mu_{\text{out}} = 6$  fm. In this figure, the side and long distributions are not shown, as they are simple Gaussians of width 5 fm centered about the origin. The figure demonstrates that as the separation  $\mu_{\text{out}}$  increases, so do the extracted femtoscopic radii.





(a) (Top Left) Simple fit on simulation from THERMINATOR 2. Generated source in the (Top Right) out, (Bottom Left) side, and (Bottom Right) long directions.



(b) Temporal characteristics of the source.

**Fig. C.1:** (Color online) Extracted radius when performing a simple fit on simulation from THERMINATOR 2, along with the spatio-temporal characteristics generated by the simulation.

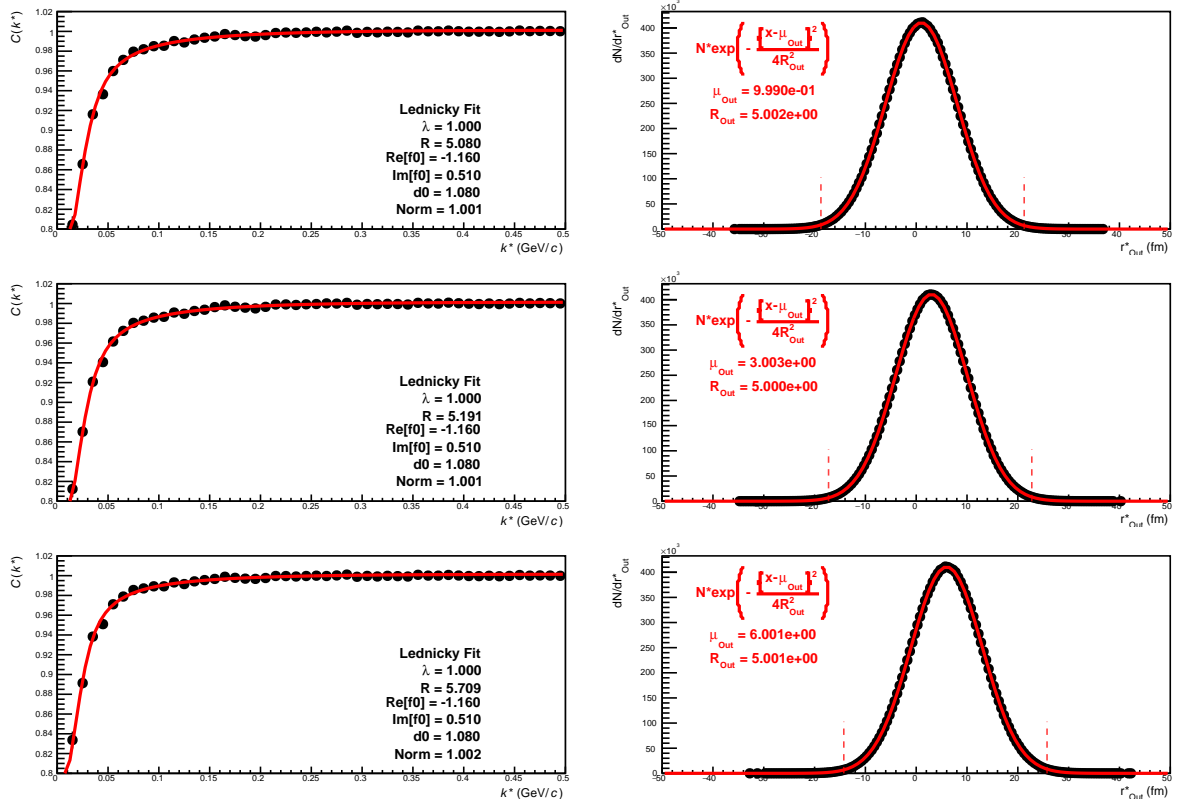


**Fig. C.2:** (Color online) Probing the effect of varying the source shift in the outward direction,  $\mu_{\text{out}}$ , within the THERMINATOR 2 framework. To achieve this, particle pairs are formed from the simulation, but with altered spatial characteristics achieved by drawing the out, side, and long components from predetermined Gaussian distributions. The plots on the left show fits resulting from the sources (in the out direction) shown on the right. The sources in the side and long directions are not shown, and are both Gaussians of width 5 fm centered at the origin for all cases. Moving from top to bottom,  $\mu_{\text{out}}$  increase from 0 to 6 fm, the effect of which clearly increases the effective radius extracted in the fit.

594 **D The ALICE Collaboration**